A New Salt-Baked Approach for Confining Selenium in Metal Complex-Derived Porous Carbon with Superior Lithium Storage Properties

Xiaona Li, Jianwen Liang, Zhiguo Hou, Wanqun Zhang, Yan Wang, Yongchun Zhu, and Yitai Qian**

For lithium-selenium batteries, commercial applications are hindered by the inferior electrical conductivity of selenium and the low utilization ratio of the active selenium. Here, we report a new baked-in-salt approach to enable Se to better infiltrate into metal-complex-derived porous carbon (Se/MnMC-B). The approach uses the confined, narrow space that is sandwiched between two compact NaCl solid disks, thus avoiding the need for protection with argon or a vacuum environment during processing. The electrochemical properties for both lithium and sodium storage of our Se/MnMC-B cathode were found to be outstanding. For lithium storage, the Se/MnMC-B cathode (with 72% selenium loading) exhibited a capacity of 580 mA h g^{-1} after 1000 cycles at 1 C, and an excellent rate capability was achieved at 20 C and 510 mA h g^{-1}. For sodium storage, a specific capacity of 535 mA h g^{-1} was achieved at 0.1 C after 150 cycles. These results demonstrate the potential of this approach as a new effective general synthesis method for confining other low melting point materials into a porous carbon matrix.

1. Introduction

In recent years, the rapidly developing market for mobile electronics, electric vehicles (EVs), hybrid electric vehicles (HEVs), and large-scale renewable energy storage has prompted the urgent need for batteries with high energy density, long cycling life and reliable stability, as well as low cost.[1,2] Nowadays, rechargeable lithium-ion batteries (LIBs) are generally used, but to meet all of the above criteria a breakthrough in the area of novel alternative rechargeable battery systems, such as metallic batteries, that is batteries with a metallic anode and a high energy cathode material, will be needed.[3–5] Considering the higher energy density of metallic batteries, lithium is the preferential choice for the anode material, because of its light weight and highly negative electrode potential. For the cathode material, both sulfur and oxygen are attractive because assembled lithium-sulfur (Li-S) and lithium-oxygen batteries have the potential of providing 2 to 5 times the energy density of the LIBs currently used.[6-8] However, there are still some problems that need to be solved before commercialization of these batteries is possible.[9-11]

Since the pioneering work by Amine in 2012,[12] lithium-selenium (Li-Se) batteries have gained attention because of their high theoretical volumetric capacity density (3253 mA h cm^{-3} based on 4.82 g cm^{-3}), which is comparable to that of Li-S batteries (3467 mA h cm^{-3} based on 2.07 g cm^{-3}).[12,13] Furthermore, Se shows several advantages over S as a cathode: 1) The intrinsic electrical conductivity of Se is higher than that of S because of its semiconductor properties,[14,15] which promises better rate performances. 2) The diminished dissolution of polyselenides and their reduced shuttle effect guarantee an improved cycling stability.[14,16,17] 3) Most reported Se cathodes have been shown to exhibit a good electrochemical performance in Li-Se batteries in less expensive carbonate-based electrolytes.[14,17-19] Thus, Li-Se batteries are promising candidates for high energy density battery systems. However, using plain Se as a cathode results in an inferior cycling stability, as well as a low Coulombic efficiency and low selenium utilization.[13]

The most commonly studied approach to solve these problems is to make Se/C composites. It is not surprising that porous carbon is the preferred choice for Se confinement because of its intrinsic good conductivity and diversity in architecture (various specific surface areas and pore distributions). The large pore volume of porous carbon provides enough space for Se loading, and the different pore textures are favorable for infiltration of the electrolyte, thus guaranteeing a fast charge transport during the cycling process. Furthermore, the high electrical conductivity ensures an efficient conductive network for the Li-Se batteries. Recently, many Se/C composites, such as Se confined in ordered mesoporous carbon,[14] hierarchical porous carbon,[20,21] and porous carbon nanospheres,[15] have been prepared to improve the electrochemical performance of Li-Se batteries by storing the active material inside the carbon matrix. Most of those reports have shown promising results

Dr. X. N. Li, J. W. Liang, Z. G. Hou, W. Q. Zhang, Y. Wang, Y. C. Zhu, Prof. Y. T. Qian
Hefei National Laboratory for Physical Science at the Microscale
Department of Chemistry
University of Science and Technology of China
96 JinZhai Road, 230026 Hefei, P. R. China
E-mail: ychzhu@ustc.edu.cn; ytqian@ustc.edu.cn

DOI: 10.1002/adfm.201501956

whereby the cycling stability, rate capacity, and specific capacity were improved.

The synthesis of selenium–carbon composites can be classified into three main categories: 1) melt-diffusion strategy in a tubular furnace under argon atmosphere flow,[20,22,23] 2) melt-diffusion strategy in a sealed vessel under argon atmosphere[14,15,21,24,25] or in vacuum.[26,27] Normally, in these two approaches, pristine Se is pre-milled together with the host porous carbon materials and then heated at around 260 °C. Because of the low viscosity of molten Se at that temperature the molten Se liquid can infiltrate into the host porous carbon materials and will be driven into the porous structures by capillary forces. However, because of the vapor pressure of the molten Se liquid there will also be a small amount of Se that is purged away by the argon flow or coagulates on the inner wall of the sealed vessel rather than being confined in the porous carbon material. Thus, the Se content in the final Se/C composites is less than the initial value in the pre-milling stage. 3) Chemical methods also exist for the synthesis of Se/C composites, which involve the reaction between the carbon source and Se[28, 29] or selenium compounds.[30] Commonly, the Se content in the final composites is relatively low (36–54%), which leads to a reduced specific energy density of the final Li-Se batteries, a factor which is crucial to the battery performance because of the limited battery packing space.[31,32] Furthermore, the cycling stability of such Se/C composites is generally not good, as only about 430 mA h g^{-1} is achieved after 250 cycles at 100 mA g^{-1}.[28]

The use of other types of carbon materials, such as one-dimensional carbon[19,33] or graphene encapsulation,[34,35] can improve the cycling stability of Se electrodes. For example, conductive graphene nanosheets wrapped Se/polyaniline (PANI) nanowires (G@Se/PANI) exhibited an enhanced cycling stability of 567.1 mA h g^{-1} at 0.2 C after 200 cycles.[35] Such approach commonly involves a complicated, multi-step process, which might only be suitable for the synthesis of a small quantity of Se electrodes. Therefore, the development of a simple and cost-effective method for the synthesis of Se/C composites is necessary.

In this study, we report a new baked-in-salt approach to have Se infiltrate better into a metal complex-derived porous carbon (Se/MnMC-B). This approach involves a process in a confined narrow space (**Figure 1**), thus avoiding the need for protection with argon or a vacuum environment. The effect of the confined narrow space is similar to the pressing process in solid-phase reactions, which facilitates the close combination of the infiltrated amorphous selenium and the porous carbon host. NaCl was selected as the confining space material, because of its high melting point and higher specific heat capacity than Se, which means that it can resist the temperature fluctuations of the external conditions to some extent. The Se/MnMC-B composite showed a specific capacity of 636 mA h g^{-1} at 0.1 C after 150 cycles. For the long cycling test, the Se/C composite delivered a capacity of 580 mA h g^{-1} at 1 C after 1000 cycles, with a capacity retention of 95.7%. When increasing the charge–discharge rate up to 20 C, a specific capacity of 510 mA h g^{-1} could be retained, which counted only for a decrease of about 20% compared to the specific capacity measured at a rate of 0.1 C. Used in sodium–selenium (Na–Se) batteries, the Se/MnMC-B electrode delivered a specific capacity of 535 mA h g^{-1} at 0.1 C after 150 cycles. It is demonstrated here that selenium might functionalize through the interaction between the Se-O bond and C-O bond to form a concomitant homogeneous adsorption on and within the porous MnMC host, thus leading to higher efficiency for Li-Se and Na-Se batteries. The main problems with the charge–discharge processes in Se electrodes, such as capacity fading, poor cycling stability, and low Coulombic efficiency, can thus be solved by using this novel approach to fabricating Se/MnMC-B electrodes.

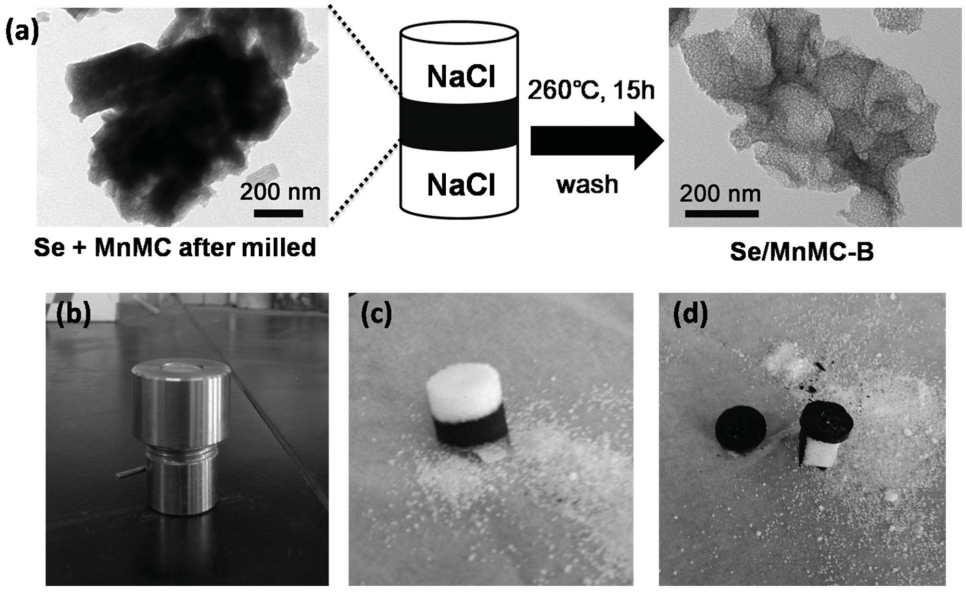

Figure 1. a) Illustration of the strategy behind the baked-in-salt approach for confining selenium in a metal complex-derived porous carbon. b) The picture of the reaction vessel (ca. 5 mL). c,d) Pictures of the mixture of Se/MnMC-B and NaCl before washing.

2. Results and Discussion

Porous carbon was synthesized by the thermal conversion of the transition metal complex, similar to our previously reported work.[36] Firstly, Mn^{2+} coordinated with the two hydroxyl oxygen atoms in malic acid to form a malic acid-Mn complex precursor ($C_4H_4MnO_5 \cdot 3H_2O$). The corresponding X-ray diffraction pattern (XRD) and scanning electron microscopy (SEM) images are shown in Figure S1 in the Supporting Information, from which we can clearly see the rod shape of the precursor. Then, after heat treatment of the malic acid-Mn complex precursor at 700 °C under Ar, followed by removal of the inorganic impurities with nitric acid, the final malic acid-Mn-derived porous carbon material (MnMC) was obtained. Figure S2b,c (Supporting Information) shows the SEM images of the as-prepared MnMC. It should be noted that the MnMC exhibited a one-dimensional rod shape, which is consistent with the shape of the malic acid-Mn complex precursor. The transmission electron microscopy (TEM) images in Figure S2d,e (Supporting Information) indicate the porous structure of MnMC. Furthermore, the microporous structure was identified by high-resolution TEM (HRTEM) (Figure S2f).

The overall strategy of the baked-in-salt approach for confining selenium in a metal complex-derived porous carbon is illustrated in Figure 1a, which consists of a common ball-milling process with subsequent melting-diffusion of selenium in a confined space, followed by a further washing process. As opposed to a melt-diffusion strategy in a tubular furnace under argon atmosphere or to a sealed-vessel strategy, the melting-diffusion process in our work is carried out in a confined space sandwiched between compacted NaCl solid disks in a sealed reaction vessel (Figure 1b). Then, after a washing process to remove the NaCl, the final Se/MnMC composites (Se/MnMC-B sample) were obtained. Temperature fluctuations could be avoided because of the much higher specific heat capacity of NaCl than Se. Thus, the whole melting-diffusion process can be finished in an almost constant-temperature system, which might be beneficial to the uniform distribution of Se in the final Se/C composites. For comparison purposes, we also prepared Se/MnMC composites by a normal melt-diffusion strategy in a tubular furnace under argon atmosphere (Se/MnMC-N sample).

The morphology and microstructure of the Se/MnMC-B composites were investigated by SEM and TEM. Compared with the precursor after the ball-milling process, as shown in Figure S3 (Supporting Information), no obvious irregular particles could be observed in the SEM and TEM images of Se/MnMC-B composites (**Figure 2**a,b), indicating that the Se was uniformly loaded in the porous carbon. The HRTEM image in Figure 2c obviously shows the disordered lattice fringes, suggesting the amorphous nature of the Se/MnMC-B composites. Both the TEM and scanning TEM (STEM) images confirm the porous structure of the Se/MnMC-B composites, which is beneficial to the fast lithium-ion transportation. Figure 2e,f displays the corresponding elemental mappings of carbon and Se, respectively. These elemental maps show that Se is dispersed homogeneously inside the porous carbon matrix and that there is no significant Se left on the surface.

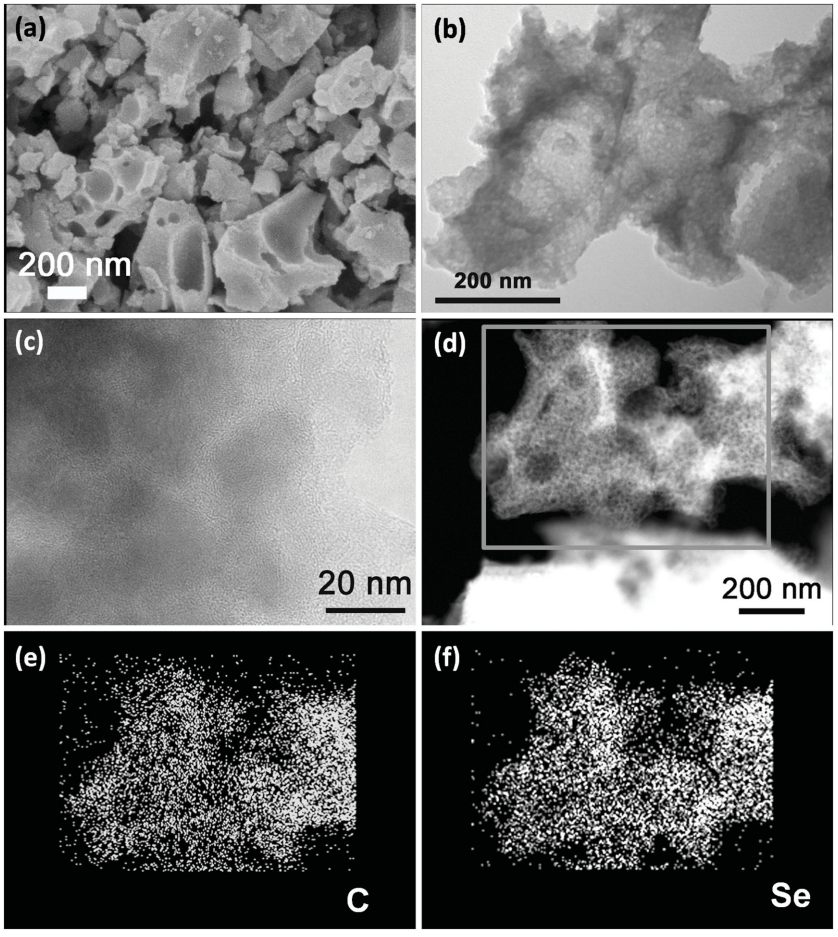

Figure 2. a) SEM, b) TEM, c) HRTEM, and d) STEM images of Se/MnMC-B composites. e,f) Se, S elemental mappings of Se/MnMC-B composites.

X-ray diffraction (XRD) patterns of the pristine bulk Se powder, Se/MnMC-B, and Se/MnMC-N composites are presented in **Figure 3**a. The XRD patterns were taken in order to understand the nature and compositional change of the products before and after the impregnation process. The XRD patterns of pristine Se and the sample after ball-milling both indicated the presence of trigonal-phase Se (JCPDS Card No. 73–0465). Whereas, after the impregnation and heat treatment, all characteristic diffraction peaks of trigonal Se disappeared, and only an amorphous structure with very broad peaks could be seen for the Se/MnMC-B and Se/MnMC-N samples, implying the nanoconfinement of Se within the MnMC host.[22] Thus, the Se in the Se/MnMC-B and Se/MnMC-N samples exists in a highly dispersed amorphous state,[14] which resulted in the high utilization of selenium during the electrochemical reaction process.

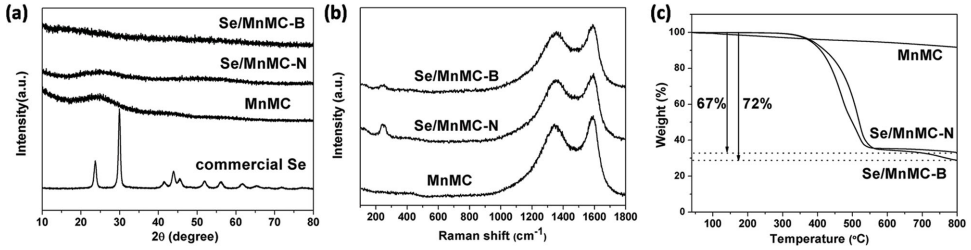

Figure 3. a) XRD patterns, b) Raman spectra, and c) TGA curves of MnMC, Se/MnMC-N, and Se/MnMC-B electrodes.

Raman spectroscopy was also used to further investigate the structural properties of Se in the Se/MnMC-B and Se/MnMC-N composites. For comparison, the Raman spectra of MnMC and bulk Se were also analyzed (Figure 3b and Figure S4, respectively). The pristine bulk Se sample displayed three peaks, the first two of which were located at 142 cm^{-1} and 458 cm^{-1} are related to ring-structured Se_{12},[37] and the peak at 235 cm^{-1} which is related to the chain-structured Se.[38] Whereas the Se/MnMC-B and Se/MnMC-N samples do not show the three characteristic peaks mentioned above. For the Se/MnMC-N sample, after having undergone the Se impregnation process, the 235 cm^{-1} peak exhibited a blue-shift to 262 cm^{-1}, which can be attributed to the ring-structured Se_8.[39] For the Se/MnMC-B sample, there was no obvious peak in the Raman spectrum, indicating the successful impregnation of Se into the MnMC pores without long-range ordering, with a possible change in the form of Se in the Se/MnMC-B sample. Those results are basically consistent with the conclusions from the XRD spectra in Figure 3a. Thus, the baked-in-salt impregnation process in confined spaces, achieved a better impregnation of Se into the pores of MnMC by capillary action. Furthermore, after the impregnation process, the amorphous nature MnMC was retained in the Se/MnMC-B and Se/MnMC-N composites. Two strong peaks at 1350 and 1600 cm^{-1} were found in the Raman spectra, which represent the D-band (disordered portion) and G-band (ordered graphitic structure), respectively, of the pores of MnMC in the composites.

As shown in Figure 3c, the TGA analyses indicate that the selenium loading in the Se/MnMC-N and Se/MnMC-B composites is 67 wt% and 72 wt%, respectively. In addition, the Se/MnMC-B sample has a higher selenium vaporizing temperature than Se/MnMC-N, indicating the strong adsorption of Se within the pores of the MnMC host. As the electrochemical performance is largely influenced by the stable confinement of Se in the porous carbon matrix,[18,40] we would expect the Se/MnMC-B to outperform the Se/MnMC-N.

Combined with the smaller amount of Se detected by X-ray photoelectron spectroscopy (XPS) on the surface of the Se/MnMC-B sample (2.59 at% for Se/MnMC-B and 11.4 at% for Se/MnMC-N, **Figure 4**a), it can be inferred that more amorphous Se is confined in the matrix of the Se/MnMC-B sample than in that of the Se/MnMC-N sample. The high-resolution C 1s XPS spectrum in Figure 4b indicates the presence of nitrogen atoms in the final Se/MnMC-B sample, with a N content of 2.8 at% on the surface. This small quantity of nitrogen might be related to the HNO_3 treatment of the MnMC host during its preparation which has been reported before. [36] The corresponding N 1s XPS spectrum of the Se/MnMC-B sample in Figure S5 (Supporting Information) demonstrates the existence of an N-X type (oxidized pyridinic) nitrogen, which might enhance the electrical conductivity of the Se/MnMC-B sample.[18,41,42] For the Se 3d spectra in Figure 4c,d the two peaks located at around 55.4 (Se 3d3/2) and around 56.2 eV(Se 3d5/2) with a spin–orbit splitting of 0.86 eV can be attributed to elemental Se.[43] One more broad peak at around 59.0 eV was observed in the Se 3d spectrum for the Se/MnMC-B sample, which is attributed to Se-O bonding, confirming the existence of SeO_2 on the surface of the Se/MnMC-B sample.[16] And the amorphous Se might be in contact with the MnMC host through interactions between the Se-O bond and the C-O bond, which could immobilize the Se and the corresponding polyselenium produced during the cycling process. Thus, the Se-O bonding might to some extent prevent the loss in activity of the Se electrodes, leading to a higher stability of the Li-Se batteries. The formation of the Se-O bonds might be due to the small amount of H_2O in the mixture of Se and MnMC before the baked-in-salt impregnation process. In the case of Se/MnMC-N, this process cannot proceed because of the Ar atmosphere, thus the trace amount of H_2O is flushed away by the Ar flow.

We investigated the lithium-storage properties of the as-prepared Se/MnMNC-B electrode in CR2016 coin cells with lithium foil as the counter electrode, and the properties of the Se/MnMNC-N electrode were also tested for comparison. **Figure 5**a shows the cyclic voltammetry (CV) curves of the Se electrode in the voltage range of 1.0–3.0 V at a sweep rate of 0.1 mV s^{-1} for the first five cycles. Based on previous reports, the electrochemical behavior of assembled Li-Se batteries differs depending on the preparation process,[15,24,26] the porous carbon hosts,[19] and the electrolytes used.[20,44] In the first discharging process, two strong peaks at around 1.75 and 1.9 V were observed, which may be related to the lithiation of different Se molecules in the Se/MnMC-B composites.[16] However, these two peaks disappeared in the second discharging process simultaneously with the appearance of a single broad reduction peak at around 1.82 V. This reduction peak shifts to a higher potential of around 1.88 V, resulting from the electrochemical activation behavior of the Se/MnMC-B electrode during the lithiation process.[19,26] On the other hand, a dominant oxidation peak at around 2.25 V was found accompanied by a small peak around 2.0 V during the whole charging process. This peak at 2.25 V becomes sharper during cycling, as shown in Figure 5a. These cathodic/anodic peaks can be ascribed to the different electrochemical reactions during cycling, demonstrating the possible formation of polyselenide intermediates or the existence of different allotropes of selenium in the Se/MnMC-B cathode.

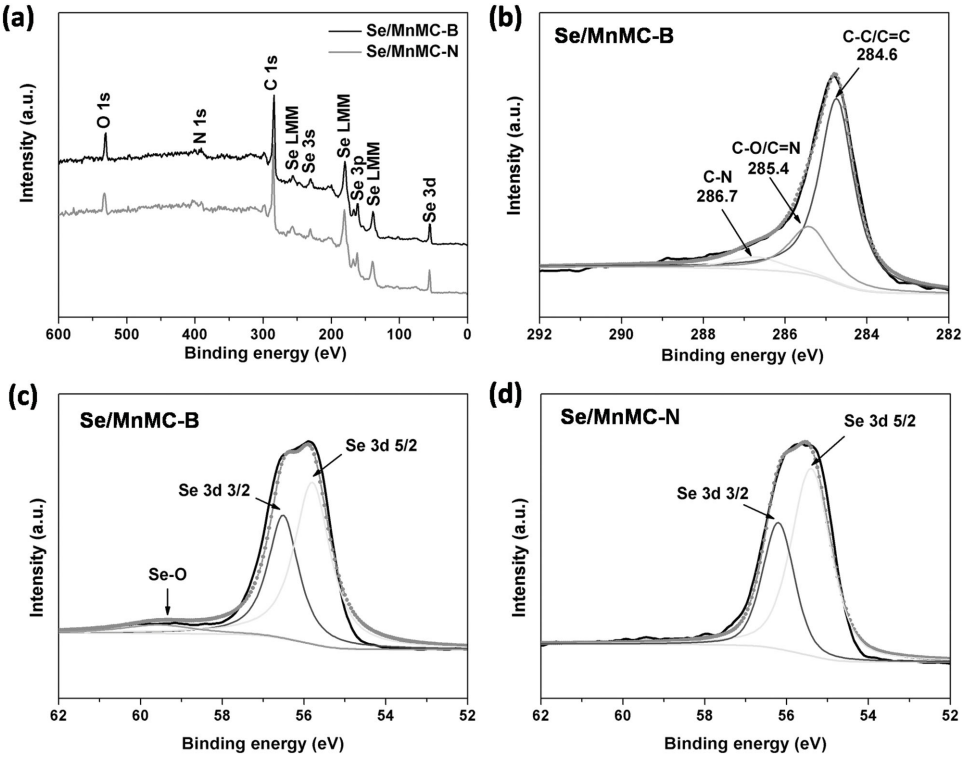

Figure 4. a) XPS spectra of Se/MnMC-B and Se/MnMC-N composites, b) C1s XPS spectrum of Se/MnMC-B. c,d) Se 3d XPS spectra of Se/MnMC-B (c) and Se/MnMC-N (d).

Figure 5b shows typical discharge–charge profiles in the first five cycles for the Se/MnMC-B electrode at 0.1 C (1 C = 678 mA g^{-1}) in the potential range of 1.0–3.0 V. The Se/MnMC-B electrode delivered initial discharge and charge capacities of 907 and 642 mA h g^{-1}, respectively, with a Coulombic efficiency of around 71%. Both the discharge and charge processes show stable voltage plateaus at around 2.0 V and behave as a single-plateau reaction. From the second cycle, the discharge/charge curves overlap well, with a stable reversible discharge capacity of 641 mA h g^{-1}, indicating that the composite cathodes possess a high reversibility and good stability. Furthermore, two small plateaus at about 2.3 and 2.1 V were observed in the first discharge of the Se/MnMC-B electrode, which is consistent with the CV curves in Figure 5a. Similar phenomena have been observed in previous reports, in which it was assumed that the small irreversible plateau was due to a molecular transformation from ring-like Se_8 to chain-like Se_n in the MnMC host during the 1st cycle.[14,15]

The rate capabilities of the Se/MnMC-B and Se/MnMC-N electrodes were investigated at C-rates from 0.1 to 20 C (**Figure 6**a,c). The discharge–charge profiles for Se/MnMC-B cathodes at various C-rates are given in Figure 6a, which shows increasingly shortened discharge-charge plateaus with increasing C-rate because of electrode polarization. It can be seen that the Se/MnMC-B electrode shows a higher initial discharge capacity (904 mA h g^{-1} at 0.1 C), than the Se/MnMC-N (896 mA h g^{-1}) sample. Also, by increasing the C rate from 0.1 to 20 C, the Se/MnMC-B electrode exhibits a higher reversible capacity and rate capability (inset of Figure 6c) than the Se/MnMC-N electrode studied in this work. The average discharge capacities of the Se/MnMC-B electrode at 0.1, 0.2, 0.5, 1, 2, 5, 10, and 20 C were 641, 626, 618, 604, 600, 575, 547, and 510 mA h g^{-1}, respectively. If the C-rate is gradually decreased back to 0.2 C, the Se/MnMC-B electrode still delivered a higher reversible discharge capacity of 620 mA h g^{-1} than that of the Se/MnMC-N electrode, which was 551 mA h g^{-1}.

Based on the rate properties of the as-prepared Se/MnMC-B and Se/MnMC-N electrodes in this context, and seeing that electron transport is the limiting step in the lithiation/delithiation process, the better rate property of the Se/MnMC-B electrode might

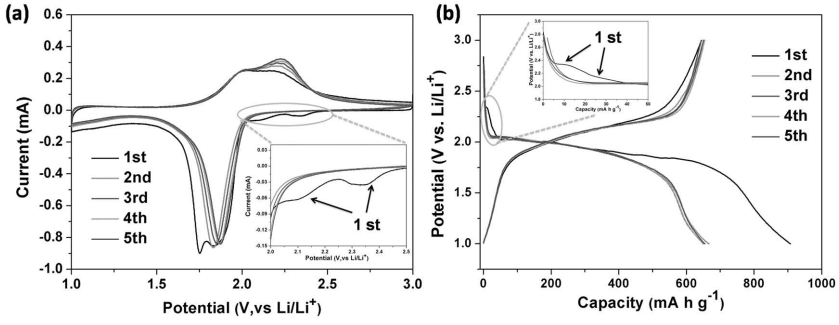

Figure 5. a) Cyclic voltammograms of the Se/MnMC-B electrode between 1 and 3 V at a potential sweep rate of 0.1 mV s^{-1}. b) Voltage profiles of the Se/MnMC-B electrode at 0.1 C (1 C = 678 mA h g^{-1}).

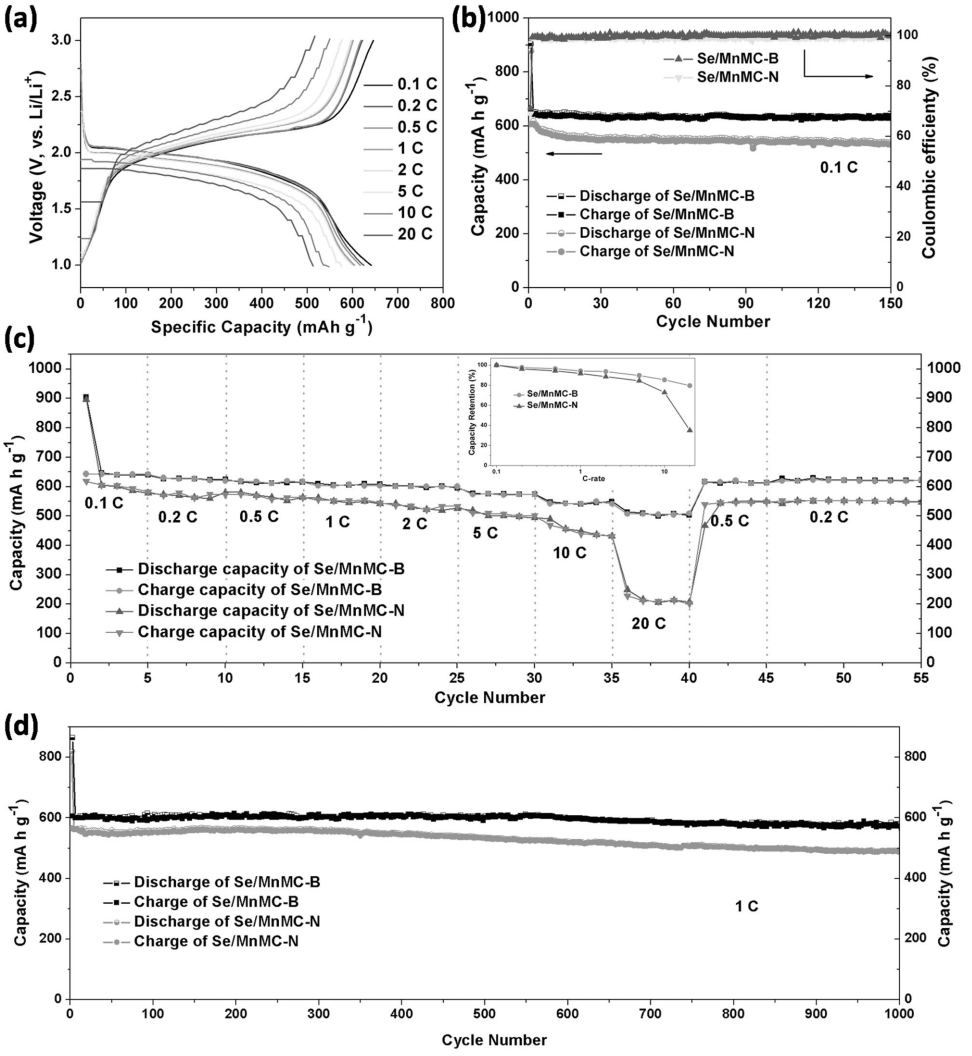

Figure 6. a) Discharge–charge profiles for Se/MnMC-B electrode at various C-rates, b) cycling performance of Se/MnMC-B and Se/MnMC-N electrodes at 0.1 C, c) rate capabilities of Se/MnMC-B and Se/MnMC-N electrodes (the inset shows the percentage capacity retention as a function of the C-rate), and d) cycling performance of Se/MnMC-B and Se/MnMC-N electrodes at 1 C.

be due to the difference in electrical conductivity. Figure S6 in the Supporting Information shows the electrochemical impedance spectroscopy (EIS) results of the as-prepared Se/MnMC-B and Se/MnMC-N electrodes before cycling. The Nyquist plots for both samples consisted of a depressed semicircle in the high- to middle-frequency region, which can be attributed to the charge-transfer resistance (R_{ct}), and a sloped line in the low-frequency region, which corresponds to the Warburg impedance. As can be seen, the semicircle diameter of the Se/MnMC-B electrode is the smallest, and a corresponding equivalent circuit model (inset of Figure S6) was constructed to analyze the impedance spectra. The fitted data are marked as dotted lines, and the simulated results were 73.5 and 128.9 Ω for the Se/MnMC-B and Se/MnMC-N electrodes, respectively. Thus, the electric conductivity of the Se/MnMC-B electrode was higher than that of the Se/MnMC-N electrode investigated in the present study, which may improve the kinetics of the processes and achieve a higher capacity and better rate capability. The better electric conductivity of the Se/MnMC-B sample might be related to the uniform distribution and the good confinement of the selenium into the porous MnMC matrix, which could provide a pathways for electron transformation.

The Se/MnMC-B and Se/MnMC-N electrodes were further subjected to testing of the cycling performance at 0.1 and 1 C. At low current density (0.1 C, Figure 6b) the reversibility of both electrodes was improved significantly, and although relatively low initial Coulombic efficiencies were obtained, these Coulombic efficiencies were increased and maintained values of above 99% from the 3th cycle onwards. The discharge capacities were stable at 636 and 537 mA h g^{-1} for the Se/MnMC-B and Se/MnMC-N electrodes, respectively, at 0.1 C after 150 cycles. Moreover, relatively long cycling tests of these two electrodes at 1 C were carried out. Figure 6d shows the initial discharge capacities of 864 and 818 mA h g^{-1} for the Se/MnMC-B and Se/MnMC-N electrodes, respectively. After 1000 cycles, a discharge capacity of 580 mA h g^{-1} was retained for the Se/MnMC-B cathode, whereas only 491 mA h g^{-1} was retained for the Se/MnMC-N electrode. Capacity retentions of 95.7 and 86.9% were

obtained from the second cycle onwards, corresponding to capacity decay rates of 0.043 and 1.31% per cycle, respectively. In spite of their differences in capacity and capacity retention, both the Se/MnMC-B and Se/MnMC-N electrodes exhibited high Coulombic efficiencies of nearly 100% because of their good structural stability during the cycling process. Even at the higher rate of 5 C, the Se/MnMC-B electrode still maintained a capacity of more than 417 mA h g^{-1} for 1000 cycles (Figure S7, Supporting Information), further indicating its superior cycling performance. Thus, the MnMC host used here not only ensured a proper and uniform Se loading, but it also facilitated electron/Li^+ transfer, inducing good cycling stability and rate capability of both electrodes.

The galvanostatic intermittent titration technique (GITT) was employed to better understand the structural transitions and the origin of the different kinetics for both electrodes during the charge/discharge process. During the GITT measurements, the Se/MnMC-B and Se/MnMC-N electrodes were charged or discharged by a series of constant current pulses of 30 mA g^{-1} with an equal duration period of 0.5 h. Then, a relaxation time of about 4 h was included between incremental charging/discharging steps in order to allow the thermodynamic equilibrium potential to be probed at different points in the charge/discharge response.

Figure 7a,b demonstrates the overall potential response profiles of the Se/MnMC-B and Se/MnMC-N electrodes, respectively, during the first cycle. The reaction resistances at different Li ion insertion and extraction levels were evaluated from the difference in potential at the end of the current step and at the end of the relaxation step, and are presented in Figure 7c. The overpotential and reaction resistances for both the Se/MnMC-B and Se/MnMC-N electrodes remain stable at first, and then rise exponentially at the end of the charging step. For the discharging process, the resistances for both electrodes decrease at first and then remain stable at the discharge platform, before finally rising again. The difference in behavior of the overpotential and reaction resistances between the charging and discharging processes might be due to the difference in reaction mechanisms between the Li^+ extraction process and the Li^+ insertion process. Furthermore, the Se/MnMC-B electrode shows a lower reaction resistance compared to that of the Se/MnMC-N sample, especially during the charge/discharge platforms, which indicates that the Se/MnMC-B electrode exhibits improved Li insertion/extraction kinetics compared to those of the Se/MnMC-N sample. This explains well the superior rate capability of the Se/MnMC-B electrode in Figure 6a,c.

Moreover, we investigated the sodium storage behavior of the Se/MnMC-B cathode (**Figure 8**). So far only a few reports have been published that refer to Na insertion in selenium materials.[19,28,29,33] Figure 8a shows the charge/discharge profiles of the Se/MnMC-B electrode at 0.1 C in the voltage range of 0.5–2.5 V for Na-Se batteries, which are similar to the curves obtained for lithium storage in Figure 5b. However, because of the different reaction potentials for Li^+ and Na^+ insertion, the output voltage of Na-Se batteries, which is about 1.7 V, is lower than that of Li-Se batteries. Moreover, there are also two small plateaus at about 2.1 and 1.9 V in the first discharge of the Se/MnMC-B electrode, which agree well with those found for the Li-Se batteries in Figure 5a,b. The Se/MnMC-B electrode

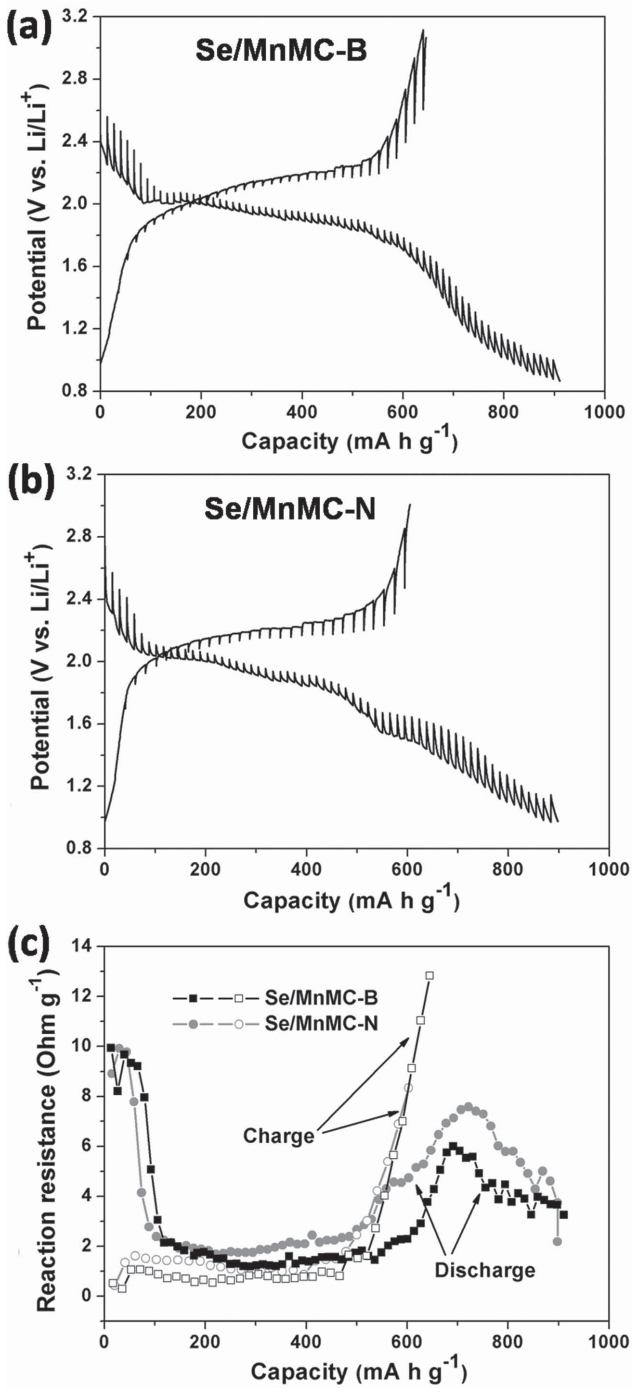

Figure 7. a,b) GITT voltage profiles of the Se/MnMC-B electrode (a) and the Se/MnMC-N electrode (b) during the first cycle. c) Reaction resistance of the Se/MnMC-B and Se/MnMC-N electrodes.

delivers initial discharge and charge capacities of 840 and 591 mA h g^{-1}, respectively, with a Coulombic efficiency of around 70%. After subsequent cycling the Coulombic efficiency increases to nearly 100%. The discharge capacity of the Se/MnMC-B electrode for Na^+ was maintained at 535 mA h g^{-1} after 150 cycles (Figure 8b). This lower capacity value might be due to the larger diameter of Na^+, which induces a lower activity

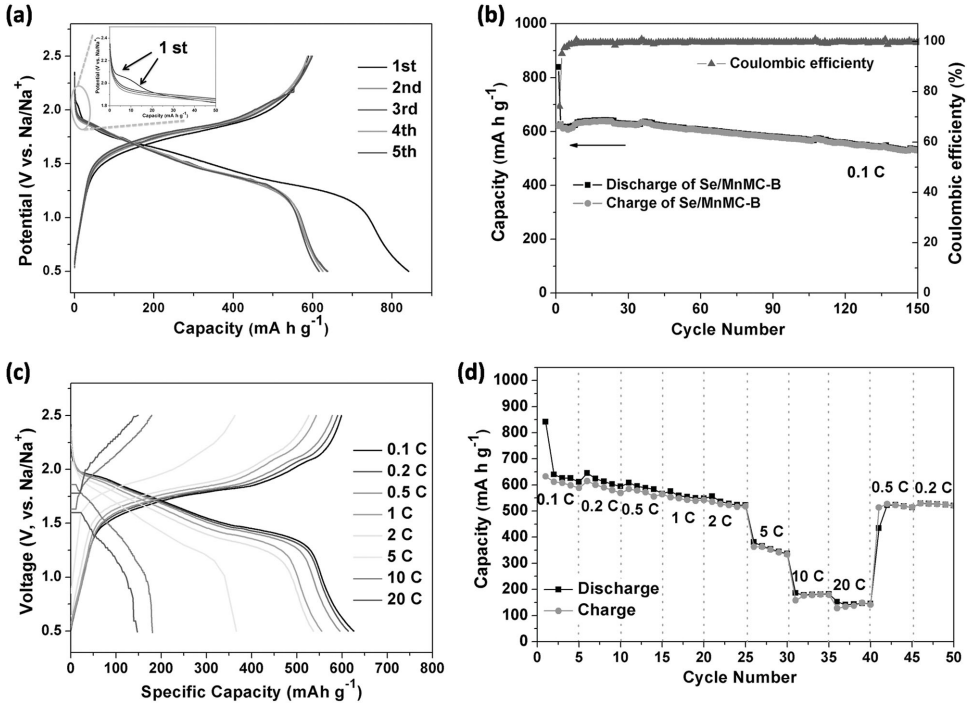

Figure 8. a) Discharge–charge profiles of the Se/MnMC-B electrode at 0.1 C in the voltage range of 0.5–2.5 V vs Na/Na^+, b) cycling performance of the Se/MnMC-B electrode at 0.1 C, c) discharge–charge profiles for the Se/MnMC-B electrode at various C-rates, and d) rate capabilities of the Se/MnMC-B electrode in a Na-Se battery.

for Na^+ insertion or de-insertion into/from the Se electrode. The corresponding rate retention is shown in Figure 8c,d. The specific capacities were 624, 613, 591, 555, 536, 365, 180, and 146 mA h g^{-1} for 0.1, 0.2, 0.5, 1, 2, 5, 10, and 20 C, respectively. The inferior rate performance compared to that of lithium storage may be caused by the sluggish Na^+ transformation at high rates.

The good cycling stability of the as-prepared Se based materials in carbonate electrolyte for both the Li-Se and Na-Se batteries agreed well with previously reported results.[24,35] We can thus conclude that the Se anions were able to react with the carbonyl groups of the carbonate solvent and that the nucleophilic Se-based electrodes worked well in the carbonate electrolyte thanks to the protection of the insulating and stable layer (similar to the solid electrolyte interphase in LIBs) on the surface.[15,43,45]

3. Conclusion

A new baked-in-salt approach has been proposed to enable the infiltration of Se into a metal complex-derived porous carbon (Se/MnMC-B), thereby avoiding the need for a protective argon or vacuum environment. The confined narrow space guaranteed the close proximity of the infiltrated amorphous selenium and the porous carbon host. The use of NaCl assured an almost constant processing temperature, because of the higher specific heat capacity of NaCl compared to that of Se, diminishing temperature fluctuations in the system. The Se/MnMC-B electrode showed an excellent electrochemical performance both for Li-Se and Na-Se batteries. For lithium storage, the Se/MnMC-B cathode showed i) a specific capacity of 636 mA h g^{-1} at 0.1 C after 150 cycles, ii) a very stable cycling performance, with a capacity of 580 mA h g^{-1} at 1 C after 1000 cycles, iii) a good rate capability delivering 510 mA h g^{-1} at 20 C. For sodium storage, a specific capacity of 535 mA h g^{-1} was achieved at 0.1 C after 150 cycles. In the Se/MnMC-B sample, selenium might be functionalized through the interaction between the Se-O bond and the C-O bond to form a concomitant homogeneous adsorption on and within the porous MnMC, thus leading to a higher efficiency for Li-Se and Na-Se batteries. The main problems of capacity fading, poor cycling stability, and low Coulombic efficiency, which are usually related to this type of battery, have thus been solved by using this preparation method. Furthermore, the results also demonstrate the great potential of this approach as a new and effective general synthesis method for confining other low melting point materials into a porous carbon matrix.

4. Experimental Section

All the chemical reagents used here were analytical grade without further purification.

Synthesis of Manganese Malate Trihydrate ($C_4H_4MnO_5{\cdot}3H_2O$) Precursor: 5 mmol of $MnCl_2{\cdot}H_2O$ and 5 mmol of malic acid were added into 40 mL ethanol in a 100 mL beaker. Then, 4 mL of 2.5 M NaOH was added dropwise to the above solution. Finally, the beaker was sealed and maintained for 6 h under ultrasonication. Then the pink product was filtered and washed with deionized water and ethanol several times, and dried under vacuum at 60 °C for 6 h.

Synthesis of Manganese Malate Derived Porous Carbon (MnMC): The as-prepared manganese malate trihydrate precursor was heated at 700 °C for 5 h in Ar atmosphere (heating rate 5 °C min^{-1}). Then, the black solid residue was washed with diluted HNO_3. Finally, the manganese malate derived carbon was collected by filtration, washed with abundant distilled water until the pH of the filtrate was about 7. The MnMC was finally dried overnight at 70 °C for 6 h in an oven.

Preparation of the Se/MnMC Composites by the Baked in Salt Approach (Se/MnMC-B Sample): In a typical synthesis, MnMC and commercial selenium with a weight ratio of 3:7 were ball-milled in a mortar for 12 h. Then the mixture was sandwiched between compacted NaCl in a 5 mL Teflon-lined stainless steel autoclave and heated to 260 °C for 24 h, at a heating rate of 2 °C min^{-1}. After the autoclave was allowed to cool down naturally to room temperature, the product was collected by centrifugation, washed with distilled water, and ethanol, and then dried under vacuum at 60 °C for 6 h.

Preparation of the Se/MnMC Composites by a Normal Melt-Diffusion Strategy (Se/MnMC-N Sample): In a typical synthesis, MnMC and commercial selenium with a weight ratio of 3:7 were ball-milled in a mortar for 12 h. Then the mixture was heated at 260 °C for 24 h at a heating rate of 2 °C min^{-1} in a tubular furnace under argon atmosphere. After cooling down to room temperature, the Se/MnMC-N composite was obtained.

Material Characterization: X-ray diffraction (XRD) was recorded on a Philips X'Pert Super diffractometer using Cu Kα radiation (λ = 1.54178 Å). The morphology of the reaction product was observed by scanning electron microscopy (SEM, JEOL-JSM-6700F), and transmission electron microscopy (TEM, Hitachi H7650 and HRTEM, JEM-ARM 200F TEM). The elemental distribution of the samples was detected by energy-dispersive X-ray spectrometry (EDX) elemental mapping analysis (JEM-ARM 200F). Raman spectra were taken on a JYLABRAM-HR confocal laser micro-Raman spectrometer. The carbon content of the product was measured by elemental analysis (EA) (Vario EL-III). Thermal gravimetric analysis (TGA) was carried out in N_2 by ramping the temperature up from room temperature to 800 °C at a heating rate of 10 °C min^{-1}. X-ray photoelectron spectroscopy (XPS) spectra were acquired on an ESCALAB 250 spectrometer (Perkin-Elmer).

Electrochemical Measurements: Electrochemical experiments were carried out using CR2016 coin cells. The electrodes were prepared by mixing the obtained materials, super P carbon, and sodium alginate (SA) binder dispersed in water at a weight ratio of 80:10:10. The obtained slurry was coated on Al foil and dried at 110 °C for 10 h in vacuum. The loading of the active materials was between 0.8 and 1.5 mg cm^{-2}. The electrolyte used for testing was 1 M $LiPF_6$ in 1:1 ethylene carbonate/diethyl carbonate (EC/DEC) (Zhuhai Smoothway Electronic Materials Co., Ltd (China)) and the separator was a Celgard 2400 membrane. The cells were assembled in an argon-filled glove box, and then aged for 12 h before testing. Galvanostatic measurements were made using a LAND-CT2001A instrument at room temperature that was cycled between 1 V and 3.0 V versus Li^+/Li at different current densities from 0.1 to 20 C (1 C = 678 mAh g^{-1}). The calculations of the specific discharge/charge capacities were based on the total mass of selenium. The AC impedance spectra were carried out using an electrochemical workstation (CHI660E) by applying an AC voltage of 5 mV in amplitude in the frequency range of 0.01 Hz to 100 kHz at room temperature. Cyclic voltammetry (CV) was carried out using a CHI660E electrochemical workstation. The obtained spectra were analyzed using ZView software. The galvanostatic intermittent titration technique (GITT) was performed under constant-current conditions for 0.5 h at a constant current density of 30 mA g^{-1}. The relaxation period was set to be 4 h. For the sodium storage test, the electrolyte was prepared by dissolving 1 M $NaClO_4$ in propylene carbonate (PC), and glass fiber (GF/D) from Whatman was used as the separator. Galvanostatic measurements were made using a LAND-CT2001A instrument at room temperature that was cycled between 0.5 V and 2.5 V versus Na^+/Na at different current densities from 0.1 to 20 C (1 C = 678 mAh g^{-1}).

Supporting Information

Supporting Information is available from the Wiley Online Library or from the author.

Acknowledgements

This work was financially supported by the 973 Project of China (No. 2011CB935901), and the National Natural Science Fund of China (No. 21471142, 21201158).

Received: May 12, 2015
Revised: June 13, 2015
Published online: July 16, 2015

[1] S. S. Zhang, *J. Power Sources* **2013**, *231*, 153.
[2] N. Jayaprakash, J. Shen, S. S. Moganty, A. Corona, L. A. Archer, *Angew. Chem. Int. Ed.* **2011**, *50*, 5904.
[3] J. B. Goodenough, Y. Kim, *Chem. Mater.* **2009**, *22*, 587.
[4] E. Yilmaz, C. Yogi, K. Yamanaka, T. Ohta, H. R. Byon, *Nano Lett.* **2013**, *13*, 4679.
[5] Y. K. Sun, D. H. Kim, C. S. Yoon, S. T. Myung, J. Prakash, K. Amine, *Adv. Funct. Mater.* **2010**, *20*, 485.
[6] M. M. Thackeray, C. Wolverton, E. D. Isaacs, *Energy Environ. Sci.* **2012**, *5*, 7854.
[7] Z. Peng, S. A. Freunberger, Y. Chen, P. G. Bruce, *Science* **2012**, *337*, 563.
[8] S. A. Freunberger, Y. Chen, Z. Peng, J. M. Griffin, L. J. Hardwick, F. Bardé, P. Novák, P. G. Bruce, *J. Am. Chem. Soc.* **2011**, *133*, 8040.
[9] P. G. Bruce, S. A. Freunberger, L. J. Hardwick, J. M. Tarascon, *Nat. Mater.* **2012**, *11*, 19.
[10] M. M. Ottakam Thotiyl, S. A. Freunberger, Z. Peng, P. G. Bruce, *J. Am. Chem. Soc.* **2012**, *135*, 494.
[11] Y. Yang, G. Zheng, Y. Cui, *Chem. Soc. Rev.* **2013**, *42*, 3018.
[12] A. Abouimrane, D. Dambournet, K. W. Chapman, P. J. Chupas, W. Weng, K. Amine, *J. Am. Chem. Soc.* **2012**, *134*, 4505.
[13] L. Liu, Y. Hou, X. Wu, S. Xiao, Z. Chang, Y. Yang, Y. Wu, *Chem. Commun.* **2013**, *49*, 11515.
[14] C. P. Yang, S. Xin, Y. X. Yin, H. Ye, J. Zhang, Y. G. Guo, *Angew. Chem. Int. Ed.* **2013**, *52*, 8363.
[15] Z. Li, L. Yuan, Z. Yi, Y. Liu, Y. Huang, *Nano Energy* **2014**, *9*, 229.
[16] H. Ye, Y. X. Yin, S. F. Zhang, Y. G. Guo, *J. Mater. Chem. A* **2014**, *2*, 13293.
[17] Y. Cui, A. Abouimrane, C. J. Sun, Y. Ren, K. Amine, *Chem. Commun.* **2014**, *50*, 5576.
[18] Y. Jiang, X. Ma, J. Feng, S. Xiong, *J. Mater. Chem. A* **2015**, *3*, 4539.
[19] L. Zeng, W. Zeng, Y. Jiang, X. Wei, W. Li, C. Yang, Y. Zhu, Y. Yu, *Adv. Energy Mater.* **2015**, *5*, 1401377.
[20] S. Jiang, Z. Zhang, Y. Lai, Y. Qu, X. Wang, J. Li, *J. Power Sources* **2014**, *267*, 394.
[21] Y. Qu, Z. Zhang, S. Jiang, X. Wang, Y. Lai, Y. Liu, J. Li, *J. Mater. Chem. A* **2014**, *2*, 12255.
[22] J. T. Lee, H. Kim, M. Oschatz, D. C. Lee, F. Wu, H. T. Lin, B. Zdyrko, W. I. Cho, S. Kaskel, G. Yushin, *Adv. Energy Mater.* **2015**, *5*, 1400981.
[23] K. Han, Z. Liu, J. Shen, Y. Lin, F. Dai, H. Ye, *Adv. Funct. Mater.* **2015**, *25*, 455.
[24] J. Zhang, L. Fan, Y. Zhu, Y. Xu, J. Liang, D. Wei, Y. Qian, *Nanoscale* **2014**, *6*, 12952.
[25] L. Liu, Y. Wei, C. Zhang, C. Zhang, X. Li, J. Wang, L. Ling, W. Qiao, D. Long, *Electrochim. Acta* **2015**, *153*, 140.
[26] Y. Liu, L. Si, X. Zhou, X. Liu, Y. Xu, J. Bao, Z. Dai, *J. Mater. Chem. A* **2014**, *2*, 17735.

[27] C. Luo, Y. Xu, Y. Zhu, Y. Liu, S. Zheng, Y. Liu, A. Langrock, C. Wang, *ACS Nano* **2013**, *7*, 8003.
[28] C. Luo, J. Wang, L. Suo, J. Mao, X. Fan, C. Wang, *J. Mater. Chem. A* **2015**, *3*, 555.
[29] H. Wang, S. Li, Z. Chen, H. K. Liu, Z. Guo, *RSC Adv.* **2014**, *4*, 61673.
[30] Z. Zhang, X. Yang, Z. Guo, Y. Qu, J. Li, Y. Lai, *J. Power Sources* **2015**, *279*, 88.
[31] H. S. Kim, T. S. Arthur, G. D. Allred, J. Zajicek, J. G. Newman, A. E. Rodnyansky, A. G. Oliver, W. C. Boggess, J. Muldoon, *Nat. Commun.* **2011**, *2*, 427.
[32] J. Gao, H. c. D. Abruña, *J. Phys. Chem. Lett.* **2014**, *5*, 882.
[33] L. Zeng, X. Wei, J. Wang, Y. Jiang, W. Li, Y. Yu, *J. Power Sources* **2015**, *281*, 461.
[34] X. Peng, L. Wang, X. Zhang, B. Gao, J. Fu, S. Xiao, K. Huo, P. K. Chu, *J. Power Sources* **2015**, *288*, 214.
[35] J. Zhang, Y. Xu, L. Fan, Y. Zhu, J. Liang, Y. Qian, *Nano Energy* **2015**, *13*, 592.
[36] X. Li, X. Zhu, Y. Zhu, Z. Yuan, L. Si, Y. Qian, *Carbon* **2014**, *69*, 515.
[37] V. V. Poborchii, *Solid State Commun.* **1998**, *107*, 513.
[38] R. Lukács, M. Veres, K. Shimakawa, S. Kugler, *J. Appl. Phys.* **2010**, *107*, 073517.
[39] Z. Lin, Z. Wang, W. Chen, L. Lir, G. Li, Z. Liu, H. Han, *Solid State Commun.* **1996**, *100*, 841.
[40] Z. Li, Y. Jiang, L. Yuan, Z. Yi, C. Wu, Y. Liu, P. Strasser, Y. Huang, *ACS Nano* **2014**, *8*, 9295.
[41] C. O. Ania, V. Khomenko, E. Raymundo Piñero, J. B. Parra, F. Beguin, *Adv. Funct. Mater.* **2007**, *17*, 1828.
[42] S. Biniak, G. Szymański, J. Siedlewski, A. Światkowski, *Carbon* **1997**, *35*, 1799.
[43] Y. Cui, A. Abouimrane, J. Lu, T. Bolin, Y. Ren, W. Weng, C. Sun, V. A. Maroni, S. M. Heald, K. Amine, *J. Am. Chem. Soc.* **2013**, *135*, 8047.
[44] C. Wu, L. Yuan, Z. Li, Z. Yi, R. Zeng, Y. Li, Y. Huang, *Sci. China Mater.* **2015**, *58*, 91.
[45] C. Luo, Y. Zhu, Y. Wen, J. Wang, C. Wang, *Adv. Funct. Mater.* **2014**, *24*, 4082.